

Listen to the Waves: Using a Neuronal Model of the Human Auditory System to Predict Ocean Waves

Artur Matysiak^a, Volker Roeber^{b,c}, Henrik Kalisch^{*c}, Reinhard König^a, and Patrick J.C. May^{†e}

^aResearch Group Comparative Neuroscience, Leibniz Institute for Neurobiology, Brennekestr. 6, 39118 Magdeburg, Germany

^bUniversité de Pau et des Pays de l'Adour, E2S-UPPA, chair HPC-Waves, SIAME, Allée du parc Montaury, 64600 Anglet, France

^cDepartment of Oceanography, University of Hawaii at Manoa, 1000 Pope Road, Honolulu, HI 96822, USA

^dDepartment of Mathematics, University of Bergen, Postbox 7800, 5020 Bergen, Norway

^eDepartment of Psychology, Lancaster University, Lancaster LA1 4YF, United Kingdom

Abstract. Artificial neural networks (ANNs) have evolved from the 1940s primitive models of brain function to become tools for artificial intelligence [1]. They comprise many units, artificial neurons, interlinked through weighted connections. ANNs are trained to perform tasks through learning rules that modify the connection weights. With these rules being in the focus of research, ANNs have become a branch of machine learning developing independently from neuroscience. Although likely required for the development of truly intelligent machines, the integration of neuroscience into ANNs has remained a neglected proposition [2]. Here, we demonstrate that designing an ANN along biological principles results in drastically improved task performance. As a challenging real-world problem, we choose real-time ocean-wave prediction which is essential for various maritime operations. Motivated by the similarity of ocean waves measured at a single location to sound waves arriving at the eardrum, we redesign an echo state network to resemble the brain's auditory system. This yields a powerful predictive tool which is computationally lean, robust with respect to network parameters, and works efficiently across a wide range of sea states. Our results demonstrate the advantages of integrating neuroscience with machine learning and offer a tool for use in the production of green energy from ocean waves.

1 Artificial neural networks.

Functionality is bestowed upon an artificial neural network (ANN) through connection weights that optimize the input-output mapping of the network in a task-specific way. The primary computational cost of using ANNs therefore arises from the need to change the connection weights according to various learning rules. Favored by the increasing availability of scalable computing resources, larger networks with many layers, so called deep neural networks, are now routinely

*henrik.kalisch@uib.no

†p.may1@lancaster.ac.uk

employed to deal with complex tasks and very large data sets [3, 4]. However, computational cost remains an issue of practical concern. For example, while it may be possible for a proof-of-concept study to use a deep neural network running on hundreds of CPUs, the same cannot be done for a system deployed, for example, in an autonomous car or in a drone. Computational cost needs to be kept low while achieving high accuracy if real-time operational support is to be provided for stabilization or navigation. In an effort to improve both accuracy and efficiency, neural networks have recently been coupled with various physical laws, encoded through partial differential equations [5, 6]. For example, encoding Galilean invariance as a multiplicative layer in a neural network enabled a realistic model of turbulent flows featuring rotational invariance [7] which is fundamental in any turbulence closure, but not naturally respected by a neural network model.

Here, we demonstrate a different route to ANN efficiency. We return to the original spirit of ANN development by adapting results from neuroscience in network design and operation. As an example of a challenging real-world problem, we take time series prediction, specifically the generation of phase-resolved forecasts of ocean surface elevation in shallow water. Real-time prediction of ocean waves is essential in marine operations and for energy production at sea [8]. In particular, the viability of wave power installations using designs such as arrays of point absorbers, flap-type converters, or oscillating water column converters depends on maximizing the efficacy of the devices with respect to real-time wave conditions. Indeed, it is well understood that the energy take-up of wave energy converters (WECs) depends critically on the oscillating structure being in resonance with the incoming ocean waves. In many cases, this alignment can be achieved using active hydraulic or electro-magnetic control of the device. The control algorithm depends on information about the incoming wave profile, and there are a number of methods which can be used to obtain this information. Since regulating the WEC appropriately requires wave-by-wave information, phase-resolving wave modeling should be used. However, standard phase-resolving models are computationally too costly to be useful in an operational fashion in this situation. As an alternative, wave measurements by radar, survey buoy, or pressure gauges could be performed continuously during operation. Radar or Lidar measurements over a large swath of the sea may still necessitate propagating the waves to the location of the WEC numerically. On the other hand, measurements in close proximity to the device requires prediction of the signal for up to 60 seconds into the future in order to allow for control adjustment. Various strategies exist for dealing with this problem [9]. In deep water, it was shown that standard Auto Regression (AR) signal analysis methods are optimal, and that ANN methods are not needed [10]. In shallower water, however, where the waves exhibit strongly nonlinear behavior, ANN methods are expected to outperform standard linear signal analysis techniques. Hence, in this work, we focus on wave-by-wave predictions in shallow water.

As our starting point, we use an echo state network (ESN), a computationally lean approach for predicting dynamical time series [11]. In ESNs, the input is fed into an ANN - the reservoir - which excites an output unit. Contributing to a low computational cost, the internal weights in the reservoir are kept fixed and only the output weights are updated during training. For this purpose, regression is used for minimizing the error between the output signal and the training signal. As a result of training, the output of the network traces the training signal. The input is then switched off and replaced with the output signal, at which point the ESN starts to generate a prediction of the time series. The term “echo” refers to the state of the reservoir encoding not just the incoming signal but also the signal’s recent history. In the current study, we refashion the ESN to make it resemble the brain’s auditory system, thereby strongly improving predictive performance.

2 Redesigning the echo state network to resemble the auditory system

While standard ESNs (stdESNs) rely on a reservoir of randomly connected units receiving the input signal directly, in the present contribution, we suggest an alternative approach where the reservoir is structured like the auditory cortex and the input is preprocessed similarly as in the cochlea of the ear. This approach is motivated by two considerations. First, as its input, the auditory system deals with streams of one-dimensional time series: the sound waves hitting each ear drum. The situation is therefore analogous to dealing with real-time ocean elevation data measured at discrete locations: in both cases, a one-dimensional time series is sampled at a single location. Second, the sound wave vibrations of the present moment only make sense when perceived against the backdrop of what came before in a time window stretching seconds into the past. A case in point is the perception of speech and music which implies that the brain must represent sounds in the context of a continuously updated representation of the recent past. This is indeed what we find in auditory cortex, where responses show strong context effects [12, 13, 14]. This kind of mixing of the current signal with the past encoded in the network state is precisely what an ESN does.

In the auditory system [15], the three-dimensional sound wave field is sampled at the eardrum whose vibrations are then amplified by the middle ear and transduced into electro-chemical signals in the cochlea of the inner ear (Fig. 1A). The cochlea carries out a spectral analysis of the sound signal, transforming its representation into a frequency mapping, the tonotopic map. Here, each neuron is maximally responsive to a specific frequency, and the best frequencies are systematically organized along one spatial dimension of the nerve tissue. Thus, the spatial pattern of cells responding to a sound encodes the frequency content of that sound. The tonotopic mapping is retained at each stage of the auditory pathway as neural activity makes its way through the brainstem and the midbrain to cortex. The auditory cortex comprises several tonotopically organized fields which differ in number, size, and connectedness across species. Despite this variability, there is a shared general hierarchical organization (Fig. 1B): At the center are the core fields, which receive the subcortical input from the auditory pathway, specifically from the medial geniculate nuclei of the thalamus. The signal then propagates to a set of belt fields surrounding the core, and from there to parabelt fields. This forward spread of activity is carried by feedforward connections, and these are complemented by feedback connections.

The above aspects are captured by a computational model of auditory cortex [16, 17, 18, 19] which we use as the basis for designing the reservoir of the ESN (see appendix A). The basic unit in the model is a representation of a cortical column comprising two mean-field neurons [20], one excitatory, the other inhibitory. A key feature of the model is its anatomical structure which mimics the hierarchical core-belt-parabelt organization of the auditory cortex. This structure is similar among mammals although the number of fields and their connectivity is species-specific [21, 22]. The dynamics of the model are described by pairs of coupled differential equations for the state variables of the excitatory and the inhibitory neurons (Eq. (2)). The column units are connected according to a matrix (Fig. 1C) which roughly replicates the connectome of the primate auditory cortex [23]. The diagonal stripes indicate tonotopic organization; the connections above and below the main diagonal are feedback and feedforward connections, respectively. This model accounts for the event-related field [16, 19] as well as for a plethora of experimental observations such as the forward enhancement of neural responses [12], the suppression of neural responses caused by stimulus repetition [13], and enhanced responses elicited by unpredictable stimuli [14]. Observations such as these show that, as a general principle, the response to the stimulus represents an interaction between the sensory inputs and the internal state of the cortex which encodes the recent past [24].

In the auditory-cortex-based ESN (audESN), the input signal first passes through a filter bank realized by a Fast Fourier Transform (FFT), thus mimicking the spectral transformation of the signal in the cochlea. The real part of the FFT is used as input to the excitatory units of the

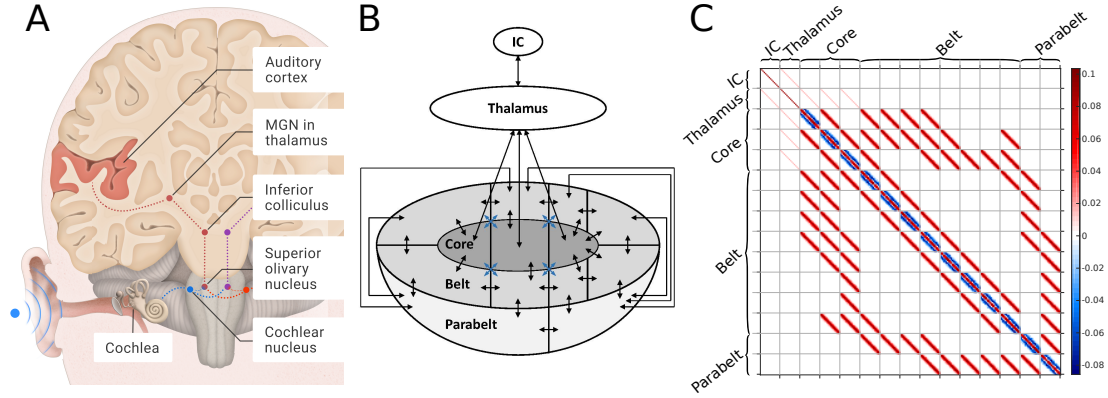


Figure 1: Modeling the auditory cortex. (A) In the auditory system, sound waves are transduced in the cochlea into electric signals. These propagate up the auditory pathway to the auditory cortex via the cochlear nucleus and the superior olivary nucleus in the brainstem as well as the inferior colliculus (IC) and the medial geniculate nucleus (MGN) in thalamus as part of the midbrain. (B) Schematic view of the primate auditory cortex [23] and the two midbrain components. The input from the ascending auditory pathway, i.e. from IC and thalamus, arrives in the core area comprising three tonotopically organized fields. The core fields are surrounded by eight belt fields and two parabelt fields. The black and blue arrows indicate reciprocal connections between fields, with high or low density of connections, respectively. (C) The structure of the auditory cortex in (B) is represented as a connection matrix, which can be used to simulate the functioning of auditory cortex. In this model, each field comprises multiple units, and each dot in the matrix representation shows a connection between two units. The superposition of two matrices indicating excitatory-to-excitatory connections and excitatory-to-inhibitory connections are shown [16] (for details, see appendix A). The color bar on the right represents the strength of the connections between any two columns: positive values (in red) stand for excitatory, negative values (in blue) for inhibitory connections (adapted from Hajizadeh et al. [16]).

AC network, while the imaginary part acts as input to the inhibitory units, thus reflecting the low-frequency and phase-dependent nature of ocean waves. The resulting tonotopic representation of the signal is then fed into the reservoir which is a modification of the computational model detailed above. While the full model of the auditory cortex is fairly complex [16, 17, 18, 19], a simplified version is used in the current computations. Here, the units in audESN are organized into a core field, which receives the pre-processed input and distributes the signal to three belt fields surrounding the core field (Fig. 2A). Fields are reciprocally and topographically connected with each other, preserving the tonotopic mapping produced by the pre-processing (Fig. 2B). However, connections are partly random so that the precise pattern of connections between two fields is unique to that pair. Within each field, columns are connected to each other via short-distance inhibitory (Fig. 2B, right panel) and longer-distance excitatory lateral connections (Fig. 2B, left panel). Figure 3 contrasts the structured reservoir used in audESN (right panel) against a randomly connected reservoir used in a stdESN (left panel). In the stdESN, the incoming signal expressed by the blue waveform on top of that figure is fed directly into all units. In an audESN with connections between columns as introduced in Fig. 2, the incoming signal is first pre-processed by a Fast-Fourier-Transform (FFT) before it is fed to the units of the core field. The readout process is based on finding the optimal coefficients for the output unit. Regression analysis is used for minimizing the error between the input signal and the signal produced by the output unit during the initial learning phase. For both stdESN and audESN, learning is implemented in an online fashion so that even during the prediction phase, regression analysis continues simultaneously, and the weights of the output unit can be updated periodically or at any chosen time points (for details, see appendix A).

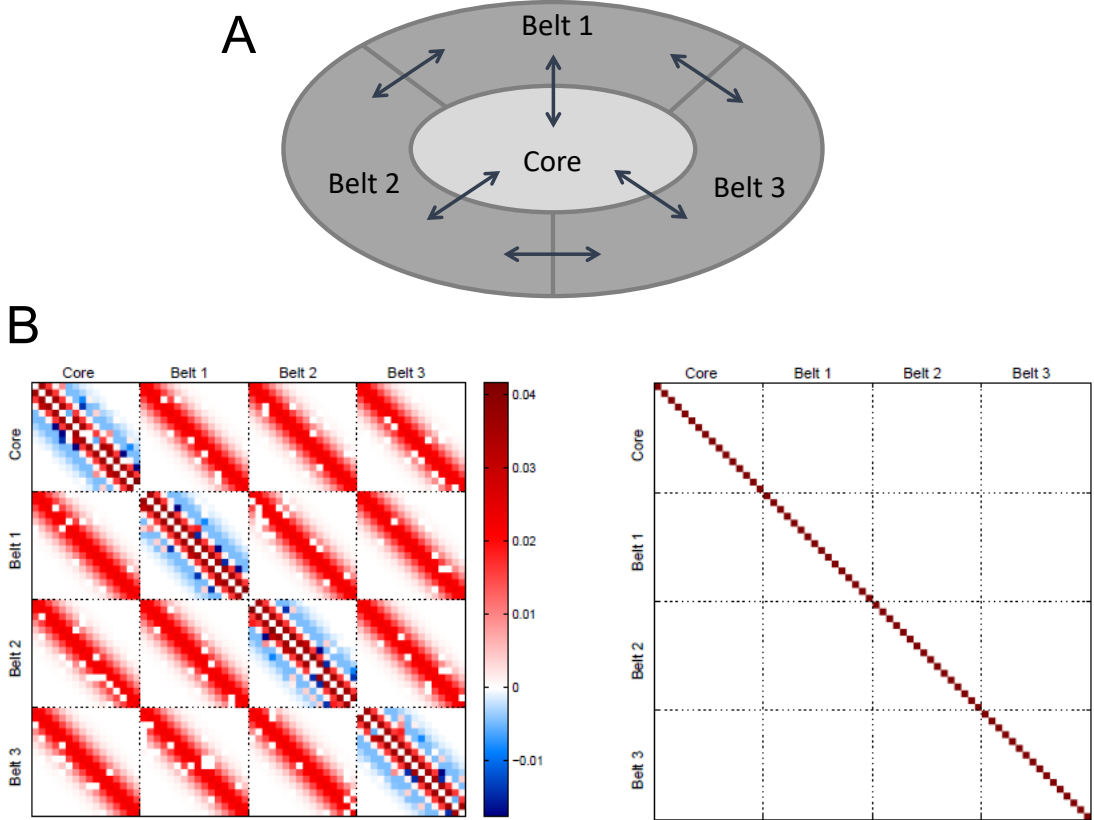


Figure 2: Simplified model of auditory cortex. (A) Schematic representation of the core-belt structure of the AC model used in the wave prediction algorithm. The single core field receives the input signal which is then distributed to three surrounding belt fields. The arrows indicate the connections between the core and belt fields. (B) The connection matrices corresponding to the four fields shown in (A) are shown (for details, see appendix A). In the case shown here, there are 16 columns per field. Each matrix element represents the strength of the connection between two columns. The left matrix shows the superposition of the matrices indicating excitatory-to-excitatory connection (W_{ee} , red) and excitatory-to-inhibitory connections (W_{ie} , blue). The matrix on the right shows the two (overlaid) diagonal matrices representing inhibitory-to-inhibitory connections (W_{ii}) and inhibitory-to-excitatory (W_{ei}) connections.

3 Prediction of ocean waves

Real-time prediction of ocean waves is essential in marine operations for stabilizing drifters and other measurement equipment and for the safe and efficient operation of wind parks and wave energy converters [8]. Early attempts to use neural network strategies for wave prediction were based on the stochastic theory of sea states [25, 26, 27]. While these techniques have matured to the point where they can be incorporated into operational wave forecasts, development continues specifically with the aim of implementing special network structures such as gated recurrent unit (GRU) models [28]. These methods do not provide phase-resolved forecasts, instead yielding estimates of average measurements of significant wave height H_s and peak period T_p with a forecasting horizon of about 24 hours.

Current neural network methods for phase-resolved wave predictions are based on deep learning [10], and as such are computationally demanding. Neural networks with low computational cost were used for wave-by-wave predictions of ocean waves in fairly deep water [29], but it was shown that they hold no clear advantage over traditional linear signal analysis methods such as auto

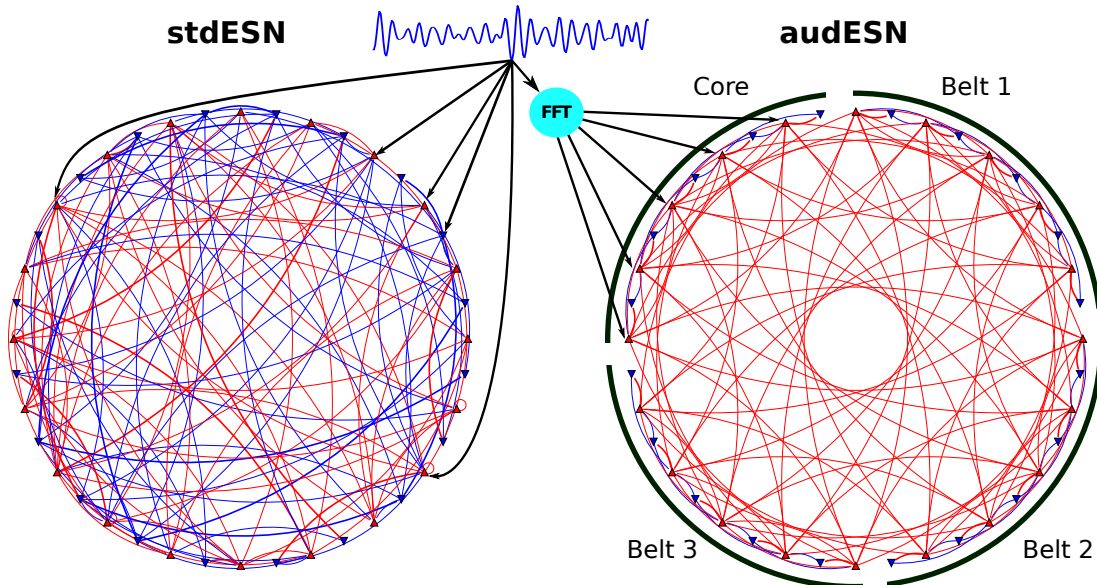


Figure 3: Structure of the reservoir. The blue waveform represents the incoming signal. On the left, the reservoir of a standard ESN (stdESN) features random connections, and the input feeds directly into all units (only five input connections shown). On the right, the simplified version of the reservoir of the auditory ESN (audESN) described in Fig. 2 is shown. The incoming signal to the audESN is first pre-processed by a Fast Fourier Transform (FFT). Red triangles and curves represent excitatory units and connections. Inhibitory units and connections are in blue. Output units are not shown.

regression techniques [10]. More recent work on phase-resolved wave forecasting focused on testing specific network architectures such as long short-term memory (LSTM) networks [30, 31]. However, this still considers waves of relatively small steepness in rather deep water where bathymetric effects and wave breaking have little to no influence. On the other hand, in shallow water, which is the focus of this work, ocean waves interact with bathymetry and exhibit highly nonlinear behavior and wave breaking, and in such an environment, predictions are much more challenging. As demonstrated here, our new method enables compelling real-time operational wave-by-wave prediction of ocean waves in shallow water.

For testing the audESN, we used simulated wave data generated with the Boussinesq Ocean & Surf Zone (BOSZ) model, a numerical modeling suite for free surface flow problems [32]. This choice was motivated by the limitations of using empirical field data. This kind of data can be difficult to classify due to imperfect sea states, missing data due to equipment failure and other potential issues. Moreover, a given location may exhibit only a very narrow range of possible sea states. In contrast, BOSZ allows for the simulation of a broad range of sea conditions, and the generated data can be easily grouped into clean sea states which is convenient for running performance comparisons such as those in the current study. With BOSZ, fast and detailed computations of wave-by-wave processes over large domains are possible and wave breaking is modeled realistically. A brief description of this model is given in appendix B. Simulations were obtained for a range of sea states with significant waveheight H_s between 0.5 and 2 m, wavelengths ranging from 100 to 250 m, and peak wave period T_p from 8 to 18 s (for more details, see appendix B). The BOSZ model was initialized with a Pierson-Moskowitz spectrum in intermediate water depth, and these waves are then propagated into shallow water, where a time series at a fixed location is extracted.

Figure 4 shows an example of how the free surface elevation traced by the stdESN (top row) and the audESN (bottom row) evolves across a time window of about 37 minutes. To provide the

surface elevation to be predicted, BOSZ simulations (black curve) were performed using a wave height of 2 m and a peak wave period of 12 s. In each case, the input signal to the ESN is the surface elevation at the same location where it is predicted. After the initial 900 s training phase, training was updated online at every other wave trough. The difference in prediction performance is clearly visible in the outputs (red curves) of stdESN and audESN. This is particularly evident in the zoomed-in representation of a shorter, 50-s long time window, where the prediction accuracy of stdESN falls significantly below that of audESN, especially for larger free surface elevations.

ESNs with 16 different reservoir types were tested, comprising stdESN, audESN, and 14 intermediate versions (Fig. 5A). These reservoir types are represented by a four-digit code where each digit expresses a binary construction choice. The first digit indicates the neuron model (presynaptic: 0; postsynaptic: 1). The second digit refers to the architecture, i.e. the type of connectivity (random: 0; tonotopic: 1). The third digit expresses whether the input was in the time domain, i.e. fed directly to the reservoir (digit 0) or in the frequency domain, i.e. FFT pre-processed (digit 1). The fourth digit indicates the size of the reservoir (small: 0; large: 1). Hence, the two default stdESNs are represented by ‘0000’ (32 units) and ‘0001’ (128 units). These had the presynaptic neuron model, random connectivity between the nodes, and computations performed in the time domain. The two default audESNs are represented by ‘1110’ (small/flat) and ‘1111’ (large/hierarchical). These utilize the postsynaptic neuron model, organization into tonotopic fields, and transformation of the signal into the frequency domain. As one moves from left to right in Fig. 5A, there is a gradual transition from stdESN to audESN.

In each test, the initial training period was 900 s, and the training was subsequently updated online at every other wave trough (see appendix A). Prediction performance was quantified as the Root Mean Square (RMS) error over 1.5 h of wave data. Each column of Fig. 5A shows the prediction performance in five selected sea states indicated by the ticks on the abscissa and characterized by the significant wave height H_s and the peak period T_p . From left to right, the five sea states are: [0.5m, 8s], [1m, 8s], [1m, 10s], [1m, 12s], and [2m, 10s]. For each sea state, 125 RMS values are given. Each RMS value is for a network with a unique combination of the three network parameters that were varied: leak rate α , spectral radius ρ and maximum bias β (for details, see appendix A). Each of these was independently varied in five steps (0.1, 0.3, 0.5, 0.7, 0.9), resulting in 125 combinations.

The following observations can be noted: First, by far the lowest RMS values were obtained with the small (‘1110’) and large (‘1111’) audESN; these RMS values were much smaller than those for the corresponding stdESNs (‘0000’ and ‘0001’). The best performing network was the large audESN (‘1111’), with the hierarchical structure of four tonotopic fields. The small audESN (‘1110’) with only one single field performed slightly worse. Second, the use of the postsynaptic neuron model of audESN (first digit = 1) consistently leads to lower minimum RMS values than the presynaptic model of stdESN (first digit = 0). Third, within each network type, the larger the waves of the sea state (i.e. as one moves from left to right within each column), the larger the RMS values. In almost all cases, the largest sea state [2 m, 10 s] leads to a very large scatter of RMS values. The exception to this is the performance of the small and large audESN where the scatter remains small for all sea states.

These observations are displayed in more detail in Fig. 5B which shows the performance data for the five sea states for stdESN (‘0001’, open symbols) and audESN (‘1111’, filled symbols). The median RMS of audESN is smaller compared to the median RMS of stdESN for all sea states, although the differences between audESN and stdESN are small for small sea states. However, this difference increases with increasing sea severity (higher significant wave height) and reaches a value of about two for the largest sea state examined. Importantly, the performance of audESN shows a much larger robustness against parameter and sea-state choice, as expressed in the minute confidence intervals (CIs) compared to the large and widely distributed (CIs) obtained for stdESN, especially for the largest sea state. In general, the audESN outperformed all other configurations.

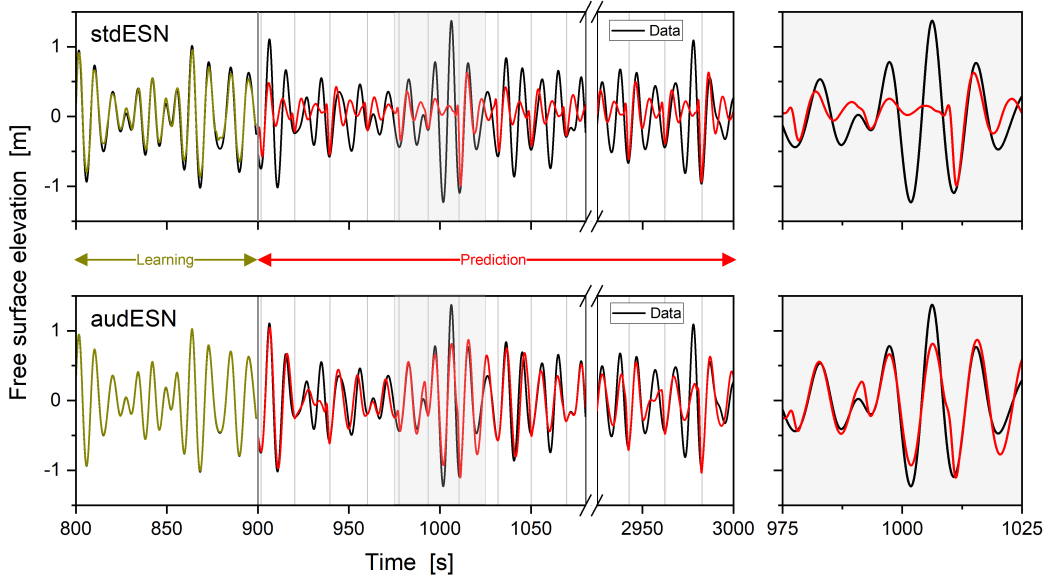


Figure 4: Prediction performance of the networks. This example shows how stdESN (top row) and audESN (bottom row) track the wave data (black curve) during training (< 900 s, green curve) and prediction (> 900 s, red curve). The network training was updated online at every other wave trough, as indicated by the vertical lines. Clearly, audESN provides much better predictions than stdESN which is evident in the two enlarged time windows shown on the right.

4 Conclusions

While the development of artificial neural networks was originally inspired by attempts to model neuronal computations [1, 2], there have not been many studies where models of the brain or other biological structures are utilized as a blueprint for the organization of an ANN [33]. As shown here for shallow water conditions, using a network based on the auditory cortex architecture and the preprocessing of the signal to represent its frequency structure gives rise to a powerful, computationally light tool for forecasting time series. This configuration mimics a biological neural network which is already optimized by natural selection to deal with single point measurements of time series data, that is, sound waves arriving at the ear. The resulting increase in operational efficiency means that the size of the network can be reduced drastically. For the predictions of ocean waves shown in Figs. 4 and 5, a network with 128 units was sufficient to provide an acceptable prediction on a forecasting horizon of two wave periods. This contrasts with other ANN methods, such as LSTM, used for generating phase-resolving predictions of ocean waves [30, 31]. In these computationally heavier networks, the number of units tends to be an order of magnitude larger, and all weights in the model are optimized, as opposed to just the output weights, as in the ESN-based approach. We note that the current ESN approach is perfectly suited for demonstrating the superiority of biological design. The fixed nature of the reservoir means that its organization - tonotopic connectivity over multiple cortical fields in this case - is retained throughout the training process. This allows for a straightforward comparison of different network structures in terms of performance. This would be more complicated with ANN methods where all the weights are optimized and where any initial setup of the internal structure is unlikely to survive the training process.

The relatively small size of the reservoir enables updating of the output weights almost instantaneously, in microseconds, through real-time simultaneous learning even during the prediction phase. In effect, audESN enables continuous operation without any need to retrain the network. In fact,

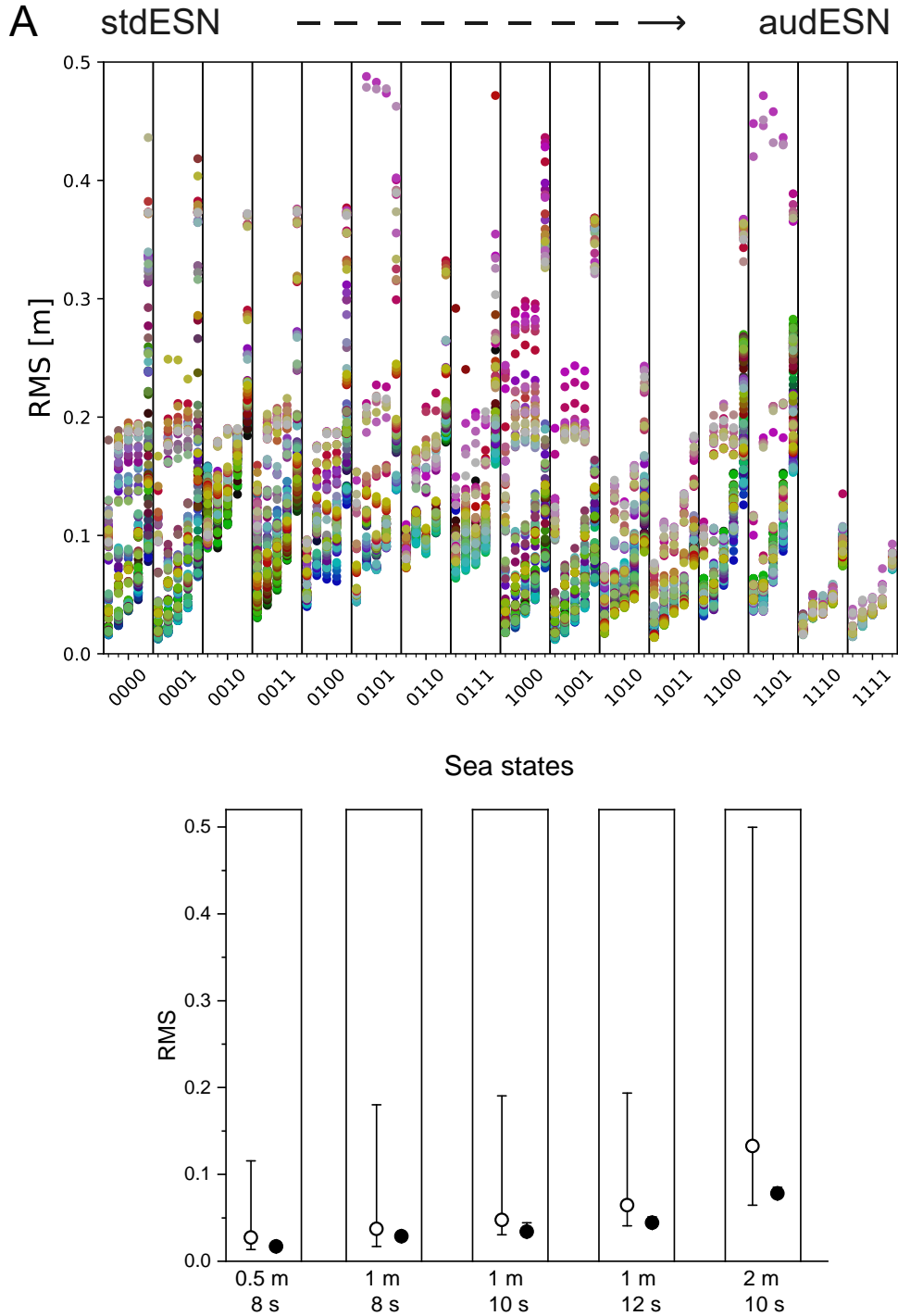


Figure 5: Prediction performance. (A) Example of the prediction performance of 16 networks. The figure shows, for each network type, the RMS error between simulated and predicted waves over 1.5 h for five sea states whose significant wave height (first row) and peak wave period (second row) are given at the bottom of the figure. For each sea state, tests were carried out for 125 combinations of the three network parameters: leak rate α , spectral radius ρ , and maximum bias β (for details, see appendix A). The four-digit codes on the abscissa denote the four binary network construction choices: neuron model, architecture, input domain, and network size (see section 3 and appendix A). (B) The median RMS errors of stdESN ('0001', open circles) and audESN ('1111', filled circles) with the corresponding confidence intervals (CIs) are shown. Among all sea states, the lowest RMS errors are achieved with audESN. Importantly, audESN also shows the best performance stability against variations in sea state and parameter choice. Note that the CIs for all five sea states are so small that they are covered by the size of the median symbol.

this special feature of constant readjustment of the network weights even in ongoing operation leads to optimal wave prediction under virtually any realistic wave conditions. In the present work, the system was tested for individual sea states, that is, under stationary conditions, but the continuous learning and online updating of the weights allow operations even under changing sea conditions. This appears to be a particularly attractive feature for the implementation of the framework for real-time wave prediction, especially near the shore. Indeed, to the best of our knowledge, no existing data-based wave prediction method has been tested in the shallow-water conditions of the nearshore zone, where bathymetric effects, nonlinear steepening, and wave breaking combine to create a highly complex wave signal. For this reason, it is difficult to make direct comparisons on performance with previous ANN approaches that have focused on predictions in deep-water conditions [30, 31].

Due to the good performance in shallow-water conditions and the robustness with regard to both reservoir parameters and sea states, there is no need for ensemble forecasts. The network can be trained a priori using data generated from ocean or nearshore models such as BOSZ. The lightweight nature of the network allows operation on embedded and even handheld devices can potentially be implemented directly in hardware, and is thus ideal for deployment at sea.

The proposed analogy between ESNs and the auditory system should not be stretched too far. First, the wave periods of ocean waves are orders of magnitude longer than those of perceptible sound waves. The current ESN is not a model of the auditory cortex as such. Rather, it copies the general principle of transducing the one-dimensional input into representations on multiple frequency maps. Second, the current results do not imply that the auditory cortex actually operates like an echo-state network, with some output neurons tracing predicted activity (although this has been suggested as a possible mechanism of predictive coding in the auditory system [34]). However, the analogy does offer possibilities of further integration of neuroscience into the ESN framework. In short-term plasticity, synaptic strengths in auditory cortex change dynamically according to pre-synaptic activity [35]. This plasticity is an order of magnitude slower than the membrane and spiking dynamics, and it offers a possible memory mechanism for representing sounds over longer intervals [17, 18]. Further, amplitude modulations of sound signals are also represented in auditory cortex so that individual neurons are tuned to specific amplitude modulation frequencies [36]. Adding these features to the ESN reservoir design might allow for further improvements in performance in terms of lengthening the effective prediction window.

In the audESN approach, changes in the frequency structure of the input signal lead to maximal changes in the reservoir state. This is due to frequency being represented spatially in multiple tonotopically-organized fields and because the connections between the fields are partly random so that each field represents the signal in a unique way. Although not shown formally, the effect is to maximize the entropy of the reservoir states as well as the mutual information between the spectral structure of the input and the spatial constellation of activity in the reservoir. This approach leads to better ESN predictive ability, and we suspect that it also describes the relationship between sound structure and the activity of auditory cortex. This might explain why there are so many tonotopic, hierarchically organized fields in auditory cortex - one of the mysteries of auditory neuroscience.

Acknowledgements. We thank Jussi Åkerberg and Christopher Ridgewell at AW-Energy, Finland, for putting together and administering the consortium of researchers, which made this study possible. PM is especially grateful to CR for the discussions that germinated the idea of mixing auditory neuroscience, machine learning, and ocean wave prediction. We thank Aida Hajizadeh and Robert Klank for their help in preparing the figures, and Peter Heil for his constructive criticism of the manuscript. This work received funding from the European Union’s Horizon 2020 research and innovation programme (grant agreement no. 763959), and from the European

Regional Development Fund (ERDF; project ZS/2018/11/96066). HK acknowledges funding from Bergen Universitetsfond. VR acknowledges financial support from the I-SITE program Energy & Environment Solutions (E2S), the Communauté d’Agglomération Pays Basque (CAPB) and the Communauté Région Nouvelle Aquitaine (CRNA) for the chair position HPC-Waves.

Appendix A: Reservoir computing

A.1. Model of auditory system

The time series prediction method developed in this paper is based on replacing the randomly connected reservoir of an Echo State Network by a structured reservoir constructed in accordance with our current understanding of the auditory cortex. The auditory cortex is a complex biological system which has been under study for some time. In a series of papers, May and colleagues developed a computational model of the cortex which is able to reproduce many phenomena observed in studies of the auditory system [17, 18].

The model is based on the idiosyncratic architecture of the auditory system of primates [23]. The basic computational unit of this AC model is the canonical microcircuit, originally proposed on the basis of results from the visual cortex of cats. It consists of interacting excitatory and inhibitory cell populations, which receive afferent feedforward excitation from the thalamus. Although this is a vast simplification of real cortical columns, which have an intricate, layered structure, the model captures the basic observation whereby all neurons within a column respond in the same way to frequency input to the column, that is, they exhibit similar tuning. The weak thalamocortical input to the excitatory population is essentially amplified by strong recurrent excitation, which itself is damped by local feedback inhibition.

A central element of the original AC model is short-term synaptic depression (STSD), which is realized by modifying the excitatory connections by time-dependent depression terms that depend on presynaptic firing. Synaptic depression has a lifetime of seconds and can be considered to be a local form of memory. However, when it is introduced to a complex network, STSD leads to various adaptation phenomena as well as to emergent properties such as individual cortical units showing selectivity to the temporal structure of sound. The model explains a wide range of phenomena observed in invasive (electrophysiological) and non-invasive (magnetoencephalographic) experiments.

A.2. The standard ESN framework

In a classical ESN framework [11], the time series representing the incoming wave is fed as input to a neural network—the so-called dynamic reservoir—with fixed structure and weights, and the units of the network are connected to an output unit. In most applications, the reservoir is a network of randomly connected units of a given size N . We refer to this network as standard ESN (stdESN). During training, only the output weights are changed through linear regression, which makes ESNs computationally very efficient. After training, the output signal resembles the training signal. Once this has been achieved, the system can be used for prediction by switching off the input signal and replacing it with feedback from the output.

The state equation of an stdESN is given by

$$\dot{x}_j(t) = -\alpha x_j(t) + \tanh \left([\rho \mathbf{W} \mathbf{x}(t)]_j + \beta_j + [\mathbf{D} \mathbf{s}(t)]_j \right), \quad (1)$$

where $x_j(t)$ ($j = [1, 2, \dots, N]$) represents the dynamical behavior of the individual neurons in the reservoir with the parameters leak rate α , spectral radius ρ , and maximum bias β , whereby biases

β_j are randomly chosen from a uniform distribution $\beta_j \in \mathcal{U}(-\beta, \beta)$. The random connectivity of the neurons of the stdESN is expressed by the matrix $\mathbf{W}_{N \times N} \in \mathcal{U}(-1, 1)$ with spectral scaling $\mathbf{W} \rightarrow \mathbf{W}/\text{maxeig}(\mathbf{W})$. The stdESN is driven by an M -dimensional stimulus $\mathbf{s}_{M \times 1}(t)$ multiplied by a random input matrix $\mathbf{D}_{N \times M} \in \mathcal{U}(-1, 1)$. Matrix multiplications are given by $[\mathbf{W}\mathbf{x}(t)]_j = \sum_{l=1}^N W_{jl}x_l(t)$ and $[\mathbf{D}\mathbf{s}(t)]_j = \sum_{l=1}^M D_{jl}s_l(t)$. This ESN features what we term a *presynaptic* nonlinearity, where the nonlinear tanh function is applied to all terms except the leak term $\alpha x_j(t)$.

A.3. The auditory system ESN framework

A.3.1. Overview

Our innovation lies in designing the network to mimic the main aspects of the auditory system. To achieve this, the incoming data are pre-processed via spectral analysis using real-time Fast Fourier Transform (FFT). The output is then fed into a set of spatial frequency maps which are tonotopically organized. The units in each tonotopic map are connected to each other with a mixture of excitation and lateral inhibition, in roughly the manner one finds in the auditory system. In contrast to the full AC model used in neuroscientific research [16, 18] (see e.g. Fig. 1 of the main text), we simplified the auditory system structure used for audESN such that the reservoir comprises only four tonotopic maps, which are organized in a core-belt structure. Specifically, the central core field receives the pre-processed input and distributes the signal to three surrounding belt fields which are connected in a ring around the core, as displayed in Fig. 2A of the main text.

A.3.2. Auditory cortex dynamics

In the AC model, the dynamics are described by two coupled differential equations for the state variables of the excitatory neurons $\mathbf{u}(t)$ (indexed by subscript ‘e’) and the inhibitory neurons $\mathbf{v}(t)$ (indexed by subscript ‘i’) [20]. The equations are written in the form

$$\begin{aligned}\tau_m \dot{\mathbf{u}}(t) &= -\mathbf{u}(t) + \mathbf{W}_{ee}g[\mathbf{u}(t)] - \mathbf{W}_{ei}g[\mathbf{v}(t)] + \mathbf{I}_e(t, f) \\ \tau_m \dot{\mathbf{v}}(t) &= -\mathbf{v}(t) + \mathbf{W}_{ie}g[\mathbf{u}(t)] - \mathbf{W}_{ii}g[\mathbf{v}(t)] + \mathbf{I}_i(t, f).\end{aligned}\tag{2}$$

Here, τ_m is the membrane time constant. The connections between the neurons are expressed by four weight matrices describing the excitatory-to-excitatory (\mathbf{W}_{ee}) and excitatory-to-inhibitory (\mathbf{W}_{ie}) connections, respectively (Fig. 2B, left matrix) as well as the inhibitory-to-inhibitory (\mathbf{W}_{ii}) and inhibitory-to-excitatory (\mathbf{W}_{ei}) connections (Fig. 2B, right matrix). In terms of modeling the auditory cortex, each neuron is representative of a population of neurons within a cortical column. Excitatory neurons make connections locally, laterally within a field, as well as across fields. Inhibitory neurons make connections locally only, within the column, and therefore \mathbf{W}_{ii} and \mathbf{W}_{ei} are diagonal. The firing rates $g[\mathbf{u}(t)]$ and $g[\mathbf{v}(t)]$ for the excitatory and inhibitory neurons are sigmoid functions $g[x] = \tanh(x)$. The terms $\mathbf{I}_e(t, f)$ and $\mathbf{I}_i(t, f)$ are time- and frequency-dependent afferent inputs and target only the core area. Here we note that the size F of each field, i.e. the number of columns per field in the network, equals the number of frequencies (the window length used for FFT). The size N of the network in terms of neurons is determined by the number of fields (four), the number of columns per field (F), and the number of neurons per column (two, one excitatory and one inhibitory), so that $N = 2 * 4 * F$.

To enable a systematic comparison of audESN with stdESN as shown in Eq. (1), we multiplied the connectivity matrices \mathbf{W}_{ee} , \mathbf{W}_{ie} , \mathbf{W}_{ei} and \mathbf{W}_{ii} with a parameter ρ corresponding to the spectral radius ($\mathbf{W}_{xx} \rightarrow \rho\mathbf{W}_{xx}$), and added a parameter corresponding to the maximum bias β , that is,

the individual random biases are $\beta_e \in \mathcal{U}(-\tau_m\beta, \tau_m\beta)$ and $\beta_i \in \mathcal{U}(-\tau_m\beta, \tau_m\beta)$. The input matrices \mathbf{D}_e and \mathbf{D}_i are tonotopically organized, that is, diagonal. Hence, Eq. (2) can be transformed into

$$\begin{aligned}\tau_m \dot{\mathbf{u}}(t) &= -\mathbf{u}(t) + \rho \mathbf{W}_{ee} \tanh(\mathbf{u}(t)) - \rho \mathbf{W}_{ei} \tanh(\mathbf{v}(t)) + \beta_e + \mathbf{D}_e \mathbf{I}_e(f, t) \\ \tau_m \dot{\mathbf{v}}(t) &= -\mathbf{v}(t) + \rho \mathbf{W}_{ie} \tanh(\mathbf{u}(t)) - \rho \mathbf{W}_{ii} \tanh(\mathbf{v}(t)) + \beta_i + \mathbf{D}_i \mathbf{I}_i(f, t).\end{aligned}\quad (3)$$

Dividing Eq. (3) by τ_m and formally combining the equations of the two state variables $\mathbf{u}(t)$ and $\mathbf{v}(t)$ according to

$$\mathbf{x}(t) = \begin{bmatrix} \mathbf{u}(t) \\ \mathbf{v}(t) \end{bmatrix}_{N \times 1}$$

then leads to

$$\dot{x}_j(t) = -\alpha x_j(t) + [\rho \mathbf{W} \tanh(\mathbf{x}(t))]_j + \beta_j + [\mathbf{D}\mathbf{s}(t)]_j, \quad (4)$$

where $\alpha = 1/\tau_m$ is the leak rate. The connectivity matrices (\mathbf{W}_{ee} , \mathbf{W}_{ie} , \mathbf{W}_{ei} , \mathbf{W}_{ii}) are combined into

$$\mathbf{W} = \frac{1}{\tau_m} \begin{bmatrix} \mathbf{W}_{ee} & -\mathbf{W}_{ei} \\ \mathbf{W}_{ie} & -\mathbf{W}_{ii} \end{bmatrix}_{N \times N}$$

and spectral scaling is applied in accordance with stdESN, that is, $\mathbf{W} \rightarrow \mathbf{W}/\text{maxeig}(\mathbf{W})$. The bias terms are given by

$$\beta = \frac{1}{\tau_m} \begin{bmatrix} \beta_e \\ \beta_i \end{bmatrix}_{N \times 1}$$

and the input matrices are combined into a single matrix \mathbf{D} . Since the signal is decomposed into F frequencies (with real and imaginary parts) and feeds only into the core area, \mathbf{D} has the dimensions of the input $M = 2 * F$ times the network size N :

$$\mathbf{D}^T = \frac{1}{\tau_m} \begin{bmatrix} \mathbf{D}_e & \mathbf{0} & \mathbf{0} & \mathbf{0} & \mathbf{0} & \mathbf{0} & \mathbf{0} & \mathbf{0} \\ \mathbf{0} & \mathbf{D}_i & \mathbf{0} & \mathbf{0} & \mathbf{0} & \mathbf{0} & \mathbf{0} & \mathbf{0} \end{bmatrix}_{M \times N},$$

where the transpose of \mathbf{D} is given for readability. The multidimensional input signal is

$$\mathbf{s}(t) = \begin{bmatrix} \mathbf{I}_e(t, f) \\ \mathbf{I}_i(t, f) \end{bmatrix}_{M \times 1}.$$

Eq. (4) is equivalent to Eq. (1), however with one major difference: unlike in Eq. (1), the nonlinear tanh function is applied only to the state variable $\mathbf{x}(t)$. Thus, we say that Eq. (4) realises a neuron model with *postsynaptic* nonlinearity.

A.3.3. Network properties

Both stdESN and audESN are characterized by the following four network properties:

1) *The neuron model.* This property indicates whether it is a presynaptic (stdESN) or a postsynaptic (audESN) model. In the presynaptic case, the nonlinear (sigmoidal) firing rate function is applied after the linear summation of all units connected to a given unit has been performed. The audESN utilizes a postsynaptic neuron model, where the nonlinear sigmoidal function is applied first, prior to the multiplication with the weight matrices.

2) *Connectivity between neurons.* In stdESN, there is no predefined organization of the network; the neurons are connected randomly. In audESN, the connections between neurons follow a well-defined anatomically-inspired structure. The audESN consists of excitatory and inhibitory connections, and the neurons are organized tonotopically. Further, within each field, neighboring

neurons are more strongly connected with each other than those that are farther away from each other.

3) *Time or frequency domain.* The working domain for stdESN is the time domain, so the input to the reservoir is just the original (not Fourier-transformed) signal. In audESN, the input signal first undergoes a windowed Fourier transform, and the transformed signal is subsequently distributed tonotopically to the respective columns.

4) *The size of the network.* We used small ($N = 2 * 1 * 16$) and large ($N = 2 * 4 * 16$) networks for both stdESN and audESN. The small audESN has only a single tonotopically organised field whereas the large audESN has four, as explained above. These two therefore differ not only in size but also with regard to the absence or presence of a hierarchical organisation.

The above four properties can be realised in $2^4 = 16$ network types. We tested all these network types for their ability to forecast ocean wave signals.

A.3.4. The prediction algorithm

General description of the algorithm

For stdESN, the input representing the incoming waves is fed as a time-domain signal to all the neurons of the reservoir. In contrast, to mimic the processing of an auditory signal in the cochlea of the inner ear, the algorithm for audESN processes the input signal $s(t)$ using short-time Fourier transform in real time. As the ocean waves are low-frequency oscillations where phase plays a crucial role, we use the real part of the FFT as input to the excitatory neurons of the AC network, while the imaginary part acts as input to the inhibitory neurons:

$$[\Re(FFT(s(t))), \Im(FFT(s(t)))] \rightarrow \mathbf{s}_{M \times 1}(t). \quad (5)$$

The input drives the reservoir, whose design represents the combination of the four network properties explained in Sec. A.3.1. The readout process is based on finding the optimal weights \mathbf{R} by which the neurons are connected to the output unit (the so-called readout neuron). Regression analysis is used for minimizing the root-mean-square (RMS) error between the input signal and the signal produced by the output unit, as given by Eq. (1) and Eq. (4). Note that in the frequency domain, the one-dimensional ocean wave height signal $s(t)$ is transformed into the multidimensional signal $\mathbf{s}_{M \times 1}(t)$ according to Eq. (5).

Once the optimal ESN output weights have been determined, a prediction is made by cutting off the input to the ESN and replacing it with the output signal. The state of the reservoir continues to generate an output signal $\tilde{s}(t) = \mathbf{R}\mathbf{x}(t)$. Note that in cases where FFT is applied to the input signal $s(t)$, $x(t)$ also represents the signal in the frequency domain. To generate the output signal, the inverse FFT from the frequency domain to the time domain is applied: $\text{IFFT}(\tilde{\mathbf{s}}(t)) \rightarrow \tilde{s}(t)$. The output weights can be updated in real time with online regression, as described in the following section.

Online regression

For efficient and fast operation, the weights between the nodes of the network have to be updated continuously. Simple regression analysis requires the computation of the inverse of a matrix, which, however, can be evaded by using the following approach. Assuming the dynamics matrix will be of the form $\mathbf{X}_{t_{j+1}} = [\mathbf{x}_{t_j}, \mathbf{x}_{t_{j+1}}]$, then the online update of the regression weights \mathbf{R} with new input data points $\mathbf{s}_{t_{j+1}}$ are given by

$$\begin{aligned} \mathbf{R}_{t_{j+1}} &= (\mathbf{X}_{t_{j+1}}^T \mathbf{X}_{t_{j+1}} + r\mathbf{I})^{-1} \mathbf{X}_{t_{j+1}}^T \mathbf{s}_{t_{j+1}} \\ \mathbf{X}_{t_{j+1}}^T \mathbf{X}_{t_{j+1}} + r\mathbf{I} &= \mathbf{X}_{t_j}^T \mathbf{X}_{t_j} + \mathbf{x}_{t_{j+1}} \mathbf{x}_{t_{j+1}}^T + r\mathbf{s}_{t_{j+1}}. \end{aligned}$$

Defining the matrix $\mathbf{P}_{t_i} = (\mathbf{X}_{t_i}^T \mathbf{X}_{t_i} + r\mathbf{I})^{-1}$ we get

$$\mathbf{P}_{t_{j+1}}^{-1} = \mathbf{P}_{t_j}^{-1} + \mathbf{x}_{t_{j+1}} \mathbf{x}_{t_{j+1}}^T.$$

Using matrix inversion $(\mathbf{A} + \mathbf{BCD})^{-1} = \mathbf{A}^{-1} - \mathbf{A}^{-1}\mathbf{B}(\mathbf{C}^{-1} + \mathbf{DA}^{-1}\mathbf{B})^{-1}\mathbf{DA}^{-1}$ with $\mathbf{A} = \mathbf{P}_{t_j}^{-1}$, $\mathbf{B} = \mathbf{x}_{t_{j+1}}$, $\mathbf{C} = \mathbf{I}$ and $\mathbf{D} = \mathbf{x}_{t_{j+1}}^T$, the update can be expressed as

$$\mathbf{P}_{t_{j+1}} = \mathbf{P}_{t_j} \left(\mathbf{I} - \frac{\mathbf{x}_{t_{j+1}} \mathbf{x}_{t_{j+1}}^T \mathbf{P}_{t_j}}{1 + \mathbf{x}_{t_{j+1}}^T \mathbf{P}_{t_j} \mathbf{x}_{t_{j+1}}} \right),$$

where $1 + \mathbf{x}_{t_{j+1}}^T \mathbf{P}_{t_j} \mathbf{x}_{t_{j+1}}$ is a scalar. One can also simultaneously downgrade previous data points to have an n -windowed regression, that is

$$\mathbf{P}_{t_{j-n}} = \mathbf{P}_{t_j} \left(\mathbf{I} + \frac{\mathbf{x}_{t_{j-n}} \mathbf{x}_{t_{j-n}}^T \mathbf{P}_{t_j}}{1 - \mathbf{x}_{t_{j-n}}^T \mathbf{P}_{t_j} \mathbf{x}_{t_{j-n}}} \right).$$

When the next data point $\mathbf{y}_{t_{j+1}}$ arrives, the updated weights $\mathbf{R}_{t_{j+1}}$ are

$$\mathbf{R}_{t_{j+1}} = \mathbf{P}_{t_{j+1}} \mathbf{X}_{t_{j+1}}^T \mathbf{s}_{t_{j+1}}.$$

This procedure avoids the explicit, time consuming calculation of the matrix inversion of $\mathbf{P}_{t_{j+1}}$.

Online spectral analysis

For efficient updating of the prediction in the frequency domain, a sliding window of F samples moving across the time series is applied. At each update, one does not need to compute the whole FFT across the window. Instead, to compute the FFT at $t = t_{i+1}$, one can utilize the FFT computation from the previous time step $t = t_i$.

$$\text{FFT}(\mathbf{s}_{[t_{i-n+1}, t_{i+1}]})_k = -i(\text{FFT}(\mathbf{s}_{[t_{i-n}, t_i]})_k + (s_{t_{i+1}} - s_{t_{i-n}}))e^{i2\pi f_k}$$

for a given frequency f_k . This procedure, combined with the above online regression method allows for rapid, on-the-fly updating of the system while it is in the prediction phase.

A.3.5. Wave-by-wave predictions

We systematically investigated the prediction performance of 16 different types of ESN, the comprised stdESN, audESN, as well as 14 intermediate network types, as explained in Sec. A.3.1. As data, we used the simulated waveforms computed with the BOSZ approach as explained in appendix B. The prediction error between the data and the predicted waves was expressed in terms of RMS values. Since the computation of the weight matrices involves random terms, the stability of our results was checked by generating multiple instances of each network type. The main findings are summarized in Figs. 5A and 5B.

Appendix B: The BOSZ model for nearshore wave modeling

B.1. Background

The Boussinesq Ocean & Surf Zone model *BOSZ* has been developed to facilitate the assessment of nearshore wave processes with a reasonable balance between accuracy and computational cost.

The solution of a depth-integrated Boussinesq-type equation returns the free surface elevation and horizontal flow velocities in the two-dimensional horizontal plane, which leads to a significant reduction in computational effort. The phase-resolving nature of the model allows for the solution of wave-by-wave processes and provides a platform to study nonlinear nearshore wave processes on the order of a wave scale such as shoaling, refraction, wave breaking, wave run-up, and recirculation.

The idea behind a Boussinesq-type approach is the removal of the vertical velocity component of the governing equations through depth-integration while retaining low-order accuracy of the vertical variation in pressure. This pseudo-3D solution is often sufficient for nearshore waves which are mostly driven by the hydrostatic pressure, i.e. the water depth. The solution of a Boussinesq-type equation can be obtained in a fraction of time in comparison to a full 3D equation with reasonable accuracy for all major processes on the scale of individual waves.

In the present study, the *BOSZ* model was employed for the calculations of 123 hypothetical wave scenarios, which provide the foundation for the training process of the stdESN and audESN. The 123 cases are representative for sea states commonly encountered along coastlines worldwide.

B.2. Wave scenarios for training of stdESN and audESN

The *BOSZ* model is used to populate a database of synthetic wave regimes based on characteristic values of peak periods, T_p , and significant wave heights, H_s . The peak period is the inverse of the frequency, at which a wave spectrum has its maximum value. The significant wave height is defined as the average of the highest 1/3 of all individual waves equal $4\sqrt{m_0}$, with m_0 denoting the zeroth moment of a wave spectrum.

Large swell waves with long peak periods are produced by strong winds over a long fetch. The wave regime is irregular and chaotic in the generation area, i.e. where a storm occurs. Subsequently, the dispersion relation controls the propagation of the individual waves in dependence of their wave length and period. This causes a process of sorting as long waves travel faster than short waves. Consequently, a sequence of individual waves observed far away from their generation area will look very much alike, whereas waves in closer proximity to a storm will differ in terms of their period. Low amplitude and long period waves are often a characteristic sign of forerunners as they get to a distant location before the main swell package arrives. It is natural that the waves at the coast exhibit different peak periods and wave heights depending on the location of the wind field.

In this study, we use 123 realistic combinations of H_s and T_p as input into an empirical Pierson-Moskowitz function. This produces sets of plausible distributions of power spectral density, which are then converted to a series of wave amplitudes with different periods as input for the *BOSZ* model. The wavemaker source term in *BOSZ* then produces an irregular free surface and velocity evolution, which resemble the spectral distribution defined by the Pierson-Moskowitz function.

In general, a wide range of combinations of H_s and T_p is possible. We have selected a range from 8 s to 20 s for the peak periods and from 0.5 m to 6.5 m for the significant wave heights. A total of 123 individual model runs was then computed over a one-dimensional straight slope of 1/20. The computational domain was 4000 m long and composed of 800 grid cells with 5 m cell size. The water depth ranges from 30 m offshore to 5 m.

A series of wave gauges is placed along the slope ranging from 1000 m to 3500 m in intervals of 50 cells. The first gauge is at the toe of the slope and last gauge is at the end of slope. The depth changes by 2.5 m between every gauge. However, in the current study, only the last gauge is used which is located at the near-end of the slope in 5 m depth. The first and last 50 cells of the domain are used for a sponge layer to absorb the outgoing waves in both directions, i.e. no run-up on dry bed is calculated to avoid reflections. The wavemaker source is centered at 500 m. The computed time for each scenario was 2 hours and the output at the wave gauges was saved at a 1 Hz sampling rate.

The slope leads to typical nonlinear processes such as wave shoaling and generation of higher

harmonics, which cause a deformation of the initially generated linear waves in terms of vertical and horizontal asymmetry. For some of the events wave breaking occurs towards the end of the slope in shallow water.

Most numerical computations depend significantly on input and boundary conditions. In our model, the wavemaker builds on the theoretical concept presented in Wei et al. [37]. The idea behind this approach is to decompose an amplitude spectrum into multiple individual monochromatic waves and then generate every single one periodically with a random phase. We start off with the definition of the empirical Pierson-Moskowitz spectrum, for which only H_s and T_p have to be known. The lowest frequency is $\frac{1}{30}$ Hz which is commonly used as limiting frequency of the gravity wave spectrum. The highest frequency depends essentially on the dispersion properties of the numerical model and its governing equation. Many Boussinesq-type equations, such as the one found by Nwogu [38] which is used here, are accurate for non-dimensional wavenumbers up to around π . The solution does not necessarily break down for shorter waves but starts developing errors in the waves' celerity. We therefore truncate the spectrum at $kh = \pi$, where k is the wavenumber and h is the local (offshore) depth. This cut-off corresponds to a frequency of $\frac{1}{6.21}$ Hz, i.e. no shorter wave is initially generated but could theoretically occur during the computation from nonlinear interactions. The spectrum is then divided into equally-spaced frequency bins between $\frac{1}{30}$ Hz and $\frac{1}{6.21}$ Hz. The width of the frequency depends essentially on the computed time of the model run. It is crucial that the time series resulting from the superposed monochromatic waves does not repeat over the course of the computation. Otherwise artificial wave groups can contaminate the solution. With 2 hours of computed time, the frequency interval Δf for binning is 0.000139 Hz. Uniform subdivision of the spectrum between the highest and lowest frequencies results in 921 frequency bins. Logically, a longer or shorter computed time would not affect the range of frequencies but the frequency bin width and consequently the total number of waves in the generation. The wave phases are initially set as random and used consistently across all 123 model runs. Once the waves are generated, they move away from the center of the source in both directions. The offshore propagating waves are immediately absorbed by a sponge layer that mimics an open ocean boundary condition and also serves to absorb potential reflected waves from the slope.

B.3. Governing Equations

The *BOSZ* model is built around the long-established Boussinesq-type equations by Nwogu [38]. These governing equations contain the Nonlinear Shallow Water (NLSW) equations as a subset and include several dispersion terms to account for the non-hydrostatic pressure effects under periodic waves. The vertical gradient of the horizontal velocity at a reference depth z_α is expressed through a truncated Taylor series expansion in combination with the vertical irrotationality conditions $u_z = w_x$, $v_z = w_y$. These conditions are valid for depth-integrated solutions since no overturning of the free surface is possible. This allows for a quadratic approximation of the vertical velocity profile expressed in terms of only horizontal velocity components. The dispersion properties of the resulting set of equations agrees very well with Airy wave theory as long as the wavelength is larger than twice the local water depth - a condition mostly given for nearshore waves.

Like most Boussinesq-type and non-hydrostatic equations the Nwogu equations [38] were derived from the Euler equations of motion and consequently lead to a formulation of the momentum equations with fluxes and local acceleration variables in non-conservative form. This does not necessarily pose an immediate problem for continuous functions, i.e. as long as the solution of free surface and velocity is smooth and free of abrupt transitions.

Obviously, Boussinesq-type and non-hydrostatic equations were primarily developed to provide solutions for nearshore processes - a regime where wave breaking is common. The presence of wave breaking creates a flow field with both subcritical as well as supercritical regimes. At the

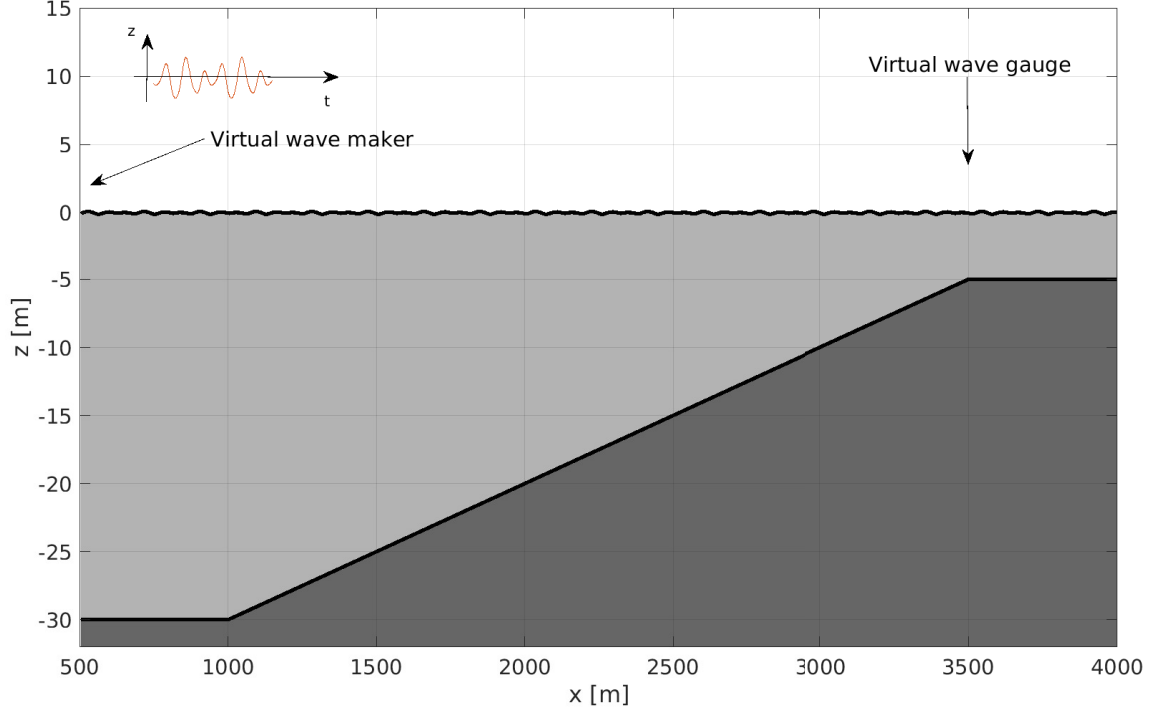


Figure 6: Schematic of the setup for the ocean wave simulations. The numerical domain has a length of 4000 m, the wavemaker is placed at a distance of 500 m from the left boundary. The toe of the slope is at 1000 m. The wave gauge used in this study was at the top of the slope, at a distance of 3500 m from the left boundary.

same time, wave breaking leads to sudden transitions in the form of shocks. The classical NLSW equations with their hyperbolic structure cater to the solution of shocks and flow discontinuities, which can be seen analogous to breaking waves. However, a correct shock solution requires that the flux terms are formulated in terms of conserved variables. This changes the units in the momentum equation terms to $[m^2/s^2]$ instead of $[m/s^2]$ and supports the mass transport across flow discontinuities. Subsequently, Roeber et al. [32] adopted this concept and reformulated the equations in conserved variables.

The equations express a balance between flux and dispersion with additional source terms. They can be cast in vector form and are shown here in x -direction only as

$$\mathbf{U}_t + \mathcal{F}(\mathbf{U})_x - \mathcal{S}_{bed} = -\mathcal{S}_{dsp} + \mathcal{S}_{frc} + \mathcal{S}_{wbr} + \mathcal{S}_{wmk} \quad (6)$$

where \mathbf{U} is the vector of conserved variables, $\mathcal{F}(\mathbf{U})$ is the flux vector, $\mathcal{S}(\mathbf{U})_{bed}$ is the bed slope source term, $\mathcal{S}(\mathbf{U})_{dsp}$ includes the dispersion terms with spatial derivatives, $\mathcal{S}(\mathbf{U})_{frc}$ accounts for bottom friction, $\mathcal{S}(\mathbf{U})_{wbr}$ is a dissipative term to account for breaking waves, and $\mathcal{S}(\mathbf{U})_{wmk}$ represents local wave generation analogous to a wavemaker paddle in a laboratory environment.

The vectors are given in differential form as

$$\mathbf{U} = \begin{bmatrix} H \\ P \end{bmatrix} \quad \mathcal{F}(\mathbf{U}) = \begin{bmatrix} Hu \\ Hu^2 + \frac{1}{2}g\eta^2 + g\eta h \end{bmatrix} \quad \mathcal{S}(\mathbf{U})_{bed} = \begin{bmatrix} 0 \\ g\eta h_x \end{bmatrix}$$

$$\begin{aligned}
\mathcal{S}(\mathbf{U})_{dsp} &= \begin{bmatrix} \psi_C \\ u\psi_C + H_t\psi_P \end{bmatrix} & \mathcal{S}(\mathbf{U})_{frc} &= \begin{bmatrix} 0 \\ \frac{gn^2u^2}{H^{1/3}} \end{bmatrix} \\
\mathcal{S}(\mathbf{U})_{wbr} &= \begin{bmatrix} 0 \\ (\nu_t H u_x)_x \end{bmatrix} & \mathcal{S}(\mathbf{U})_{wmk} &= \begin{bmatrix} \sum_{i=1}^{M_\omega} D_i \cos[k_i(x) - \omega_i t + \phi_i] \\ 0 \end{bmatrix}. \quad (7)
\end{aligned}$$

Here, H and h are the total flow depth and still water depth, respectively. u is the horizontal velocity, g is gravity, η denotes the free surface, n is the Manning roughness coefficient of units $[\text{s m}^{-1/3}]$, and ν_t is the eddy viscosity necessary for wave breaking closure. The wavemaker source term generates an oscillating superposition of individual monochromatic waves each with a random phase ϕ , magnitude D , wave number k , and angular frequency ω , over the entire computed time.

The local acceleration term in the momentum equation accounting for frequency dispersion with mixed space-time derivatives is given by

$$P = Hu + H \left[\frac{z_\alpha^2}{2} (u_{xx}) + z_\alpha (hu)_{xx} \right]$$

and the dispersion terms with only spatial derivatives are denoted by

$$\begin{aligned}
\psi_C &= \left[\left(\frac{z_\alpha^2}{2} - \frac{h^2}{6} \right) hu_{xx} + \left(z_\alpha + \frac{h}{2} \right) h(hu)_{xx} \right]_x, \\
\psi_P &= \left[\frac{z_\alpha^2}{2} u_{xx} + z_\alpha (hu)_{xx} \right],
\end{aligned}$$

where z_α is the reference depth, at which the horizontal velocity is evaluated. The position influences the dispersion properties where values closer to the free surface favor the accuracy of short wave dispersion and vice versa. Since the free surface is the result of a superposition of multiple individual waves, the reference depth has to work for a wide range of wavelengths and cannot be set simply for only one single frequency. A value around mid-depth such as $z_\alpha = -0.531h$ provides optimized shoaling and dispersion properties for a range of waves within $kh < \pi$.

B.4. Numerical Solution

The accuracy of the solution of the present Boussinesq-type formulation, with the NLSW equations as subset, benefits from conservative numerical methods. Therefore, the governing equations are solved on a collocated grid with a combination of a Finite Volume scheme for the hydrostatic part of the equations and a central differential Finite Difference scheme for the non-hydrostatic pressure correction terms. The Finite Volume scheme solves for the spatial gradients of the fluxes, $\mathcal{F}(\mathbf{U})$, and bed slope term, $\mathcal{S}(\mathbf{U})_{bed}$, based on a solution from the HLLC approximate Riemann solver at all cell interfaces. A total variation diminishing method is used as reconstruction method for the values of water depth and flow speed as input into the Riemann solver at all grid cell interfaces. As higher-order methods reduce numerical diffusion, a 5th-order reconstruction method is used.

A two-step Runge-Kutta method is then employed for the time integration, in which the evolution variables \mathbf{U}_t in Eq. (6) are discretized as

$$\begin{aligned}
\mathbf{W} &= \mathbf{U}^n + \Delta t \mathcal{L}(\mathbf{U}^n) \\
\mathbf{U}^{n+1} &= \frac{1}{2}(\mathbf{U}^n + \mathbf{W}) + \frac{\Delta t}{2} \mathcal{L}(\mathbf{W}),
\end{aligned}$$

where $\mathcal{L}(\mathbf{U})$ accounts for the variation of \mathbf{U} in all $\mathcal{F}(\mathbf{U})$ and $\mathcal{S}(\mathbf{U})$ terms of Eq. (6) at the present time step n . The auxiliary variable \mathbf{W} denotes the predicted values of \mathbf{U} which are subsequently

used in the corrector step as $\mathcal{L}(W)$ to obtain the values at U^{n+1} with second-order accuracy in time. The time step Δt varies dynamically depending on the present flow conditions in all grid cells of index i as

$$\Delta t = \frac{\Delta x}{2 \cdot \max(u_i^n + \sqrt{gh_i})}. \quad (8)$$

Eq. (8) implies the use of a Courant number of 0.5. The evolution variable in the momentum equation of Eq. (6) contains combined flux and dispersion terms together with mixed space and time derivatives. Once the evolution variables are obtained at the next time step ($n + 1$), a tridiagonal linear systems of equations is solved for the horizontal flow velocity u as the solution vector. This concludes the calculation at each time step. The procedure is repeated until the final time is reached.

B.5. Wave breaking closure

The source terms in Eq. (7) of the governing equations include a dissipative term for wave breaking $\mathcal{S}(U)_{wbr}$, without which a converging solution would not be possible. It is obvious that a depth-integrated solution cannot produce overturning of the free surface; for that a vertical discretization would be necessary. The closest solution to overturning of the wave front is a discontinuity. However, most Boussinesq-type systems do not per se allow for the formation of discontinuities since the presence of elliptic dispersion terms eliminates the purely hyperbolic structure of the underlying NLSW equations.

Often, solutions for breaking waves can be obtained by making use of some inherently present numerical diffusion. However, grid refinement ultimately reduces numerical diffusion over discrete grid cells and the solution tends to the formation of singularities at the position of the wave front. This phenomenon is mathematically and numerically correct; however, it is not the desired solution for applications.

A dissipative term added to the momentum equations can provide an efficient way to reach closure of the problem. Here, we utilize an approach which makes use of the eddy viscosity concept, a technique which provides a reasonable basis for local dissipation at the breaking wave front.

The diffusive term in the momentum equation of $\mathcal{S}(U)_{wbr}$ works in a similar fashion as the bottom friction term - though in a more complex way as it involves the time-varying eddy viscosity ν_t which controls the magnitude of the diffusion term. The magnitude of the dissipative term not only depends on the local flow variables (H and u), but also on the entire turbulent flow field represented by ν_t . It is therefore necessary that ν_t has a physical basis, since a fixed coefficient does not account for the variations in the flow regime.

Nwogu [39] has developed an approach to determine the quantity of turbulent kinetic energy (TKE) from a one-equation model that can be used as proxy or the assessment of ν_t in each time step. This technique was later revisited by Kazolea and Ricchiuto [40], and it is further optimized in the present work.

A relation between TKE and ν_t was defined by Pope [41] in the form

$$\nu_t = C_\nu \ell_t \sqrt{k}, \quad (9)$$

where ℓ_t is a coefficient representing the turbulence length scale which is here given by the local water depth, $\ell_t = h$. The coefficient C_ν is set to 0.55 as suggested by Kazolea and Ricchiuto [40]. The solution of Eq. (9) then requires an estimate of TKE, for which Pope [41] had formulated a general governing equation as

$$k_t = -\mathcal{A} - \mathcal{E} + \mathcal{P} + \mathcal{D}, \quad (10)$$

where \mathcal{A} , \mathcal{E} , \mathcal{P} , \mathcal{D} denote advection, elimination/destruction, production, and diffusion of TKE, denoted by k with units of $[m^2/s^2]$. \mathcal{E} and \mathcal{D} are generally rather small quantities and most of the solution of TKE is controlled by the production term \mathcal{P} .

We assume that turbulence is produced where wave breaking occurs. Since overturning of the free surface is not possible in depth-integrated equations, finding a robust definition of wave breaking is notoriously difficult. Here, we make use of the advantage that the governing equations (Eq. (6)) allow for a reconstruction of the horizontal velocity at the free surface as

$$u|_{\eta} = u + \frac{1}{2} (z_{\alpha}^2 - \eta^2) u_{xx} + (z_{\alpha} - z) (hu)_{xx}.$$

It is then assumed that wave breaking begins once the flow at the wave crest becomes supercritical, i.e. the horizontal velocity at the wave crest exceeds the wave celerity [42]. Therefore, \mathcal{P} is calculated locally where the criterion of $Fr \geq 1$ is met. The other terms in Eq. (10) are computed throughout the entire domain and lead to a distribution of TKE across the surf zone. Consequently, the diffusive term \mathcal{S}_{wbr} is largest at the wave breaking front. As breaking waves move to shore, some TKE is left behind the breaking crests and merges with TKE produced by subsequently breaking waves. This can be seen analogously to white water and foam production in a dissipative surf zone. The distribution of TKE helps with the convergence of solutions over a wide range of grid cell sizes without the occurrence of singularities.

The terms in Eq. (10) are detailed by Nwogu [39] and involve several empirical coefficients. Here, we express a modified version of Eq. (10) without the need for case-dependent tuning. The TKE advection term is conventionally defined as

$$\mathcal{A} = uk_x.$$

The TKE elimination/destruction term with the coefficient $C_d = (C_v)^3$ is denoted as

$$\mathcal{E} = C_d \frac{k^{3/2}}{\ell_t}$$

and the TKE diffusion term \mathcal{D} is given by

$$\mathcal{D} = \nu k_{xx},$$

where ν is the kinematic viscosity of water.

The last term necessary for closure is the term defining production of TKE. As mentioned above, it is only computed in cells where the threshold $Fr \geq 1$ is exceeded, i.e. the local quantity of $u|_{\eta}$ reaches at least \sqrt{gh} . The production term of TKE can be expressed in analogy to the Boussinesq eddy viscosity concept which relates the turbulence shearstresses to the velocity gradients:

$$\mathcal{P} = \frac{\ell_t^2}{\sqrt{C_d}} [u_z|_{\eta} \cdot u_z|_{\eta}]^{3/2}.$$

The vertical gradient of the horizontal velocities can be computed from the truncated Taylor series expansion inherent to the governing equations in combination with the vertical irrotationality condition as

$$u_z|_{\eta} = -\eta u_{xx} - (hu)_{xx}.$$

It is then understood that energetic wave breaking, such as encountered in plunging breakers, leads to an increase in the vertical gradient of the horizontal velocities under the wave crest, $u_z|_{\eta}$ and consequently to a sudden increase in \mathcal{P} . Once all components of the turbulence closure model are computed, the governing equation of TKE, Eq. (10) is integrated in time with the same Runge-Kutta scheme as the governing equations, Eq. (6) and the quantity of ν_t is dynamically determined from Eq. (9) at each time step and in each grid cell. This provides the variables for the time-varying dissipative term for wave breaking, $\mathcal{S}(U)_{wbr}$, in Eq. (7).

References

- [1] Cox, D.D., Dean, T. *Neural networks and neuroscience-inspired computer vision*, Curr. Biol. **24**, R921–R929 (2014).
- [2] Hassabis, D., Kumaran, D., Summerfield, C., Botvinick, M. *Neuroscience-inspired artificial intelligence*, Neuron **95**, 245–258 (2017).
- [3] Krizhevsky, A., Sutskever, I., Hinton, G. *ImageNet classification with deep convolutional neural networks*, Adv. Neural Inform. Proc. Syst. **25**, 1097–1105 (2012).
- [4] LeCun, Y., Bengio, Y., Hinton, G. *Deep learning*, Nature **521** (7553), 436–444 (2015).
- [5] Raissi, M., Perdikaris, P., Karniadakis, G.E. *Physics-informed neural networks: A deep learning framework for solving forward and inverse problems involving nonlinear partial differential equations*, J. Comput. Phys. **378**, 686–707 (2019).
- [6] Raissi, M., Yazdani, A., Karniadakis, G.E. *Hidden fluid mechanics: Learning velocity and pressure fields from flow visualizations*, Science **367** (6481), 1026–1030 (2020).
- [7] Ling J., Kurzawski, A., Templeton, J. *Reynolds averaged turbulence modelling using deep neural networks with embedded invariance*, J. Fluid Mech. **807**, 155–166 (2016).
- [8] Budar, K., Falnes, J. *A resonant point absorber of ocean-wave power*, Nature **256**, 478–479 (1975).
- [9] Mérigaud, A., Ramos, V., Paparella, F., Ringwood J.V. *Ocean forecasting for wave energy production*, J. Mar. Res. **75**, 459–505 (2017).
- [10] Fusco, F., Ringwood, J.V. *Short-term wave forecasting for real-time control of wave energy converters*, IEEE Trans. Sustain. Energy **1**, 99–106 (2010).
- [11] Jaeger, H., Haas, H. *Harnessing nonlinearity: Predicting chaotic systems and saving energy in wireless communication*, Science **304**, 78–80 (2004).
- [12] Brosch, M., Schreiner, C. E. *Sequence sensitivity of neurons in cat primary auditory cortex*, Cereb. Cortex **10**, 1155–1167 (2000).
- [13] Lü, Z. L., Williamson, S.J., Kaufman, L. *Human auditory primary and association cortex have differing lifetimes for activation traces*, Brain Res. **572**, 236–241 (1992).
- [14] Näätänen, R., Gaillard, A.W., Mäntysalo, S. *Early selective-attention effect on evoked potential reinterpreted*, Acta Psychol. **42**, 313–329 (1978).
- [15] Pickles, J.O. *Auditory pathways: anatomy and physiology*, Handb. Clin. Neurol. **129**, 3–25 (2015).
- [16] Hajizadeh, A., Matysiak, A., May, P.J.C., König, R. *Explaining event-related fields by a mechanistic model encapsulating the anatomical structure of auditory cortex*, Biol. Cybern. **113**, 321–345 (2019).
- [17] May, P. J. C., Tiitinen, H. *Temporal binding of sound emerges out of anatomical structure and synaptic dynamics of auditory cortex*, Front. Comput. Neurosci. **7**, 152 (2013).
- [18] May, P. J. C., Westö, J., Tiitinen, H. *Computational modelling suggests that temporal integration results from synaptic adaptation in auditory cortex*, Eur. J. Neurosci. **41**, 615–630 (2015).
- [19] Hajizadeh, A., Matysiak, A., Wolfrum, M., May, P. J. C., König, R. *Auditory cortex modelled as a dynamical network of oscillators: understanding event-related fields and their adaptation*, Biol. Cybern. **116**, 475–499 (2022).
- [20] Hopfield, J.J., Tank, D.W. *Computing with neural circuits: A model*, Science **233**, 625–633 (1986).
- [21] Baumann, S., Petkov, C.I., Griffiths, T.D. *A unified framework for the organization of the primate auditory cortex*, Front. Syst. Neurosci. **7** 11 (2013).
- [22] Budinger, E., Heil, P. *Anatomy of the auditory cortex*, In: Greenberg, S., Ainsworth, W.A., editors. Listening to speech. Mahwah, New Jersey: Lawrence Erlbaum Associates, Publishers pp. 91–113 (2005).
- [23] Hackett, T.A., de la Mothe, L.A., Camalier, C.A., Falchier, A., Lakatos, P., Kajikawa, Y., Schroeder, C.E. *Feedforward and feedback projections of caudal belt and parabelt areas of auditory cortex: Refining the hierarchical model*, Front. Neurosci. **8**, 72 (2014).
- [24] Buonomano, D.V., Maass, W. *State-dependent computations: spatiotemporal processing in cortical networks*, Nat. Rev. Neurosci. **10**, 113–125 (2009).
- [25] Deo, M., Jha, A., Chaphekar, A. S., Ravikant, K. *Neural networks for wave forecasting*, Ocean Eng. **28**, 889–898 (2001).

- [26] Londhe, S., Panchang, V. *One-day wave forecasts using buoy data and artificial neural networks*, J. Atmos. Ocean Technol. **23**, 1593–1603 (2006).
- [27] Londhe, S.N., Panchang, V. ANN Techniques: A Survey of Coastal Applications In: Advances In Coastal Hydraulics. pp. 199–234 (2018).
- [28] Yevnin, Y., Chorev, S., Dukan, I., Toledo, Y. *Short-term wave forecasts using gated recurrent unit model*, Ocean Eng. **268**, p. 113389 (2023).
- [29] Duan, W., Ma, X., Huang, L., Liu, Y., Duan, S. *Phase-resolved wave prediction model for long-crest waves based on machine learning*, Comput. Methods Appl. Mech. Eng. **372**, p.113350 (2020).
- [30] Ma, X., Duan, W., Huang, L., Qin, Y., Yin, H. *Phase-resolved wave prediction for short crest wave fields using deep learning*, Ocean Eng. **262**, p. 112170 (2022).
- [31] Meng, Z.F., Chen, Z., Khoo, B.C., Zhang, A.M. *Long-time prediction of sea wave trains by LSTM machine learning method*, Ocean Eng. **262**, p. 112213 (2022).
- [32] Roeber, V., Cheung, K.F., Kobayashi, M.H. *Shock-capturing Boussinesq-type model for nearshore wave processes*, Coastal Eng. **57**, 407–423 (2010).
- [33] Lagergren, J.H., Nardini, J.T., Baker, R.E., Simpson, M.J. and Flores, K.B. *Biologically-informed neural networks guide mechanistic modeling from sparse experimental data*, PLoS Computational Biology **16**, p.e1008462 (2020).
- [34] Wacongne, C., Changeux, J.P., Dehaene, S. *A neuronal model of predictive coding accounting for the mismatch negativity*, J. Neurosci. **32**, 3665–3678 (2012).
- [35] Fioravante, D., Regehr, W.G. *Short-term forms of presynaptic plasticity*, Curr. Opin. Neurobiol. **21**, 269–274 (2011).
- [36] King, A.J., Teki, S., Willmore, B. *Recent advances in understanding the auditory cortex*, F1000Research 7, F1000 Faculty Rev-1555 (2018).
- [37] Wei, G., Kirby, J.T. and Sinha, A. Generation of waves in Boussinesq models using a source function method *Coastal Engineering* **36**, 271–299 (1999).
- [38] Nwogu, O. Alternative form of Boussinesq equations for nearshore wave propagation. *J. Waterway, Port, Coastal and Ocean Engineering* **119**, 618–638 (1993).
- [39] Nwogu, O. G. Numerical prediction of breaking waves and currents with Boussinesq model. In *Coastal Engineering Proceedings 1996*, pp. 4807–4820 (1997).
- [40] Kazolea, M. and Ricchiuto, M. On wave breaking for Boussinesq-type models. *Ocean Modelling* **123**, 16–39 (2018).
- [41] Pope, S. B. *Turbulent flows*. Cambridge University Press, Cambridge, 2003.
- [42] Bjørkavåg, M. and Kalisch, H. Wave breaking in Boussinesq models for undular bores. *Physics Letters A*, **375**, 1570–1578 (2011).